Int J CARS (2006) 1:107–117
DOI 10.1007/s11548-006-0011-2

Four-dimensional cardiac MR tagged imaging and image processing

S. Urayama[a] · N. Sugimoto[b] · F. Jouo[b] · T. Yamamoto[c] · T. Azuma[c] · H. Fukuyama[a] · S. Tsutsumi[c] · S. Eiho[d]

[a]Human Brain Research Center, Graduate School of Medicine, Kyoto University, Japan
[b]Department Systems Science, Graduate School of Informatics, Kyoto University, Japan
[c]Department Medical Simulation Engineering, Institute for Frontier Medical Sciences, Kyoto University, Japan
[d]The Kyoto College of Graduate Studies for Informatics, Japan

Abstract Four-dimensional cardiac tagged imaging with retrospective respiratory gating and its image processing were performed A 3D-cine-TrueFISP sequence with plane-tag pulses was developed, using LISA and TARD techniques for transient-artifact reduction. For respiratory monitoring, an optical displacement sensor fixed in the gantry was used to measure the lower abdomen level during a scan. The obtained MRI raw- and respiratory-data were combined for retrospective gated reconstruction. Automatic tag-plane detection based on a quadratic approximation was applied to each 3D image. Although time resolution was relatively low (97 ms/cardiac phase), clear tag-contrast was observed on the images through a whole cardiac cycle. Almost all tag-planes being on the images could be detected with subvoxel resolution.

Keywords Respiratory-gating · Artifactless-coherent-ssfp · Subvoxel-tag-detection

1 Introduction

Regional deformation abnormalities in the heart wall provide a useful indicator of ischemia [1, 2]. Myocardial magnetization tagging is one of only a few methods for noninvasive assessment of regional myocardial deformation. However, in order to find the complex three-dimensional motion of the left ventricle (LV), tagged images must be taken of at least 8–10 slices, the tagged images must be analyzed slice by slice, and then the obtained set of 2D deformation data is integrated to find the 3D deformation of the heart wall [3]. This long imaging time, with repeated breath-holds and time-consuming image analysis, increases the difficulty of using this method clinicallly. Moreover, variation of diaphragm position between the breath-holds lowers the precision of the reconstructed 3D LV-deformation.

Our goal is therefore to develop a rapid 4D (3D-cine) MR tagged imaging without breath-holds, and an automatic 4D tagged image analysis method. In this report, we describe a method for rapid 4D tagged imaging with a combination of ECG and respiratory gating using an optical displacement sensor, and a method for automatic tag-plane detection with subvoxel resolution, based on a regional quadratic approximation with Taylor expansion.

2 Materials and methods

2.1 Data acquisition

Four-dimensional MR tagged images were taken with a 1.5 T whole body scanner (Sonata, Siemens Medical Solutions, Inc., Erlangen, Germany).

Respiratory gating was accomplished retrospectively using a optical displacement sensor (LK-500, Keyence, Osaka, Japan) whose maximum spatial and temporal resolution are 0.05 mm and 1 ms, respectively. The sensor and a mirror were fixed on a frame covering the subject so that the laser targeted the lower abdomen (Fig. 1). The abdominal motion was monitored as respiratory motion data during a scan, and it was recorded on a PC with 10 ms temporal resolution.

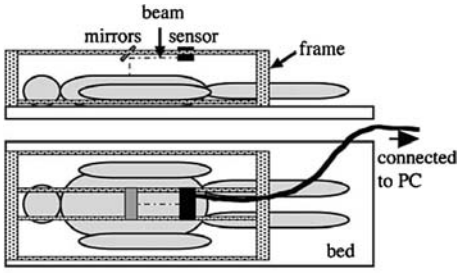

Fig. 1 Respiratory sensor system. The optical displacement sensor and mirror was positioned on a frame which covers the subject's body. Laser output from the sensor targetted the lower abdomen of the subject via mirror reflection and addomen surface motion with respiratory was monitored in the vertical direction

A conventional cine-TrueFISP sequence [4] was extended for 3D-cine imaging and magnetization tagging. A parallel-plane tag pattern, which is perpendicular to the readout direction, was produced with 8 mm spacing, just after R-wave detection in the ECG signal. Since the tag-planes deformation in a set of 4D tagged images only provides the regional heart wall motion component along the readout direction, three sets of 4D images were taken with their readout directions along three orthogonal ones, one of which was parallel to the long axis of LV and the other two were orthogonal to it. In the following part, these sets of 4D images are called ''LA'', ''SA1'' and ''SA2'' images, respectively, because the imaged planes are so-called long-axis-view and short-axis-views, respectively. In order to obtain sufficient signal-to-noise ratio, each 4D data set was measured with ten repetitions. For reduction of the initial artifact of TrueFISP sequence which can be observed in images taken less than about 100 ms after the tagging pulses, TARD (Transient Artifact Reduction with Dispersion of phase) [5] and LISA (Linearly Increasing Startup Angles) [6] methods were also applied. For the retrospective respiratory gating, raw data was recorded and the 4D images were reconstructed off-line as described in the next part. Other imaging parameters are summarized in Table 1.

2.2 Image reconstruction

We here provide a brief and simple explanation of the raw data in MRI, so-called ''k-space''. The k-space can be considered as a frequency domain, in contrast to the reconstructed images as a space domain. In this study, the number of dimensions of k-space included was three; the directions of the 3D space represented the readout, phase-encoding and partition (slice-thickness) directions, respectively. The number of k-space data sets is the product of the number of cardiac phases and that of the receiver coils, i.e., $(7 \times 4 = 28)$ k-space sets were used for each image set in this study. A reconstructed 3D image at a given cardiac phase can be obtained by applying the Fourier transform to each k-space data set at the cardiac phase, calculating the magnitude value at each voxel and then adding all the magnitude images from different coils.

The structure of a raw data file obtained within a single scan is a series of a mini-header and 1D-data along the readout direction of the k-space, in acquisition order. A mini-header contains information about the 1D-data, e.g., cardiac phase, coil number, phase-encoding number, partition number and time stamp at which the data is measured. From these information, the 1D-data can be restored to the appropriate

Table 1 Imaging parameters

Parameters	SA	LA1	LA2
TR (ms)	3.13	3.13	3.35
TE (ms)	1.57	1.57	1.68
FOV (mm)	360 × 169 × 96	360 × 236 × 120	360 × 281 × 120
Acquisition matrix (pixels)	256 × 70 × 30	256 × 70 × 39	256 × 87 × 39
Image matrix (pixels)	256 × 120 × 64	256 × 186 × 80	256 × 232 × 80
Tag interval (mm)	8		
Voxel size (mm)	1.4 × 1.4 × 1.5		
# CardiacPhase	7		
CardiacPhase Interva (ms)	97		
Coil	body array (two channels) and spine array (two channels)		
Scan time (s)	90	117	156
Total scan time (h)	1.5		

position of the particular k-space. Also, from the time stamp, the respiratory level (related to the excursion of the lower abdomen) at the moment of data acquisition can be found from the respiratory monitor data, and a decision can be made whether or not the data are to be discarded. In this study, for the retrospective respiratory gating, a range of the respiratory levels, which was determined from the histogram of the observed levels, was applied for this decision.

2.3 Image processing

Tag-plane detection with subvoxel resolution was accomplished with a quadratic approximation, using a Taylor expansion. Signal change near a voxel center, $\mathbf{x}$, of the original 3D image, $f(\mathbf{x})$, can be approximated by

$$\begin{aligned} f(\mathbf{x}+\mathbf{dx}) &\cong f(\mathbf{x}) + \nabla f \cdot \mathbf{dx} + 0.5 \cdot^{\mathrm{T}} \mathbf{dx} \cdot \mathbf{H} \cdot \mathbf{dx} \\ &= 0.5 \cdot \sum_{i=1}^{3} \lambda_i \left(\mathbf{dx} \cdot \mathbf{v}_i + \frac{(\nabla f \cdot \mathbf{v}_i)}{\lambda_i} \right)^2 \\ &\quad + f(\mathbf{x}) - 0.5 \cdot \sum_{i=1}^{3} \frac{(\nabla f \cdot \mathbf{v}_i)^2}{\lambda_i} \end{aligned} \tag{1}$$

where ∇f is the first derivative of $f(\mathbf{x})$, $\mathbf{H}$ is the Hesse matrix whose components are second derivatives, λ_i (i = 1,2,3, $|\lambda_1| \geq |\lambda_2| \geq |\lambda_3|$) are the eigenvalues of $\mathbf{H}$ and $\mathbf{v}_i$ (i = 1,2,3, $|\mathbf{v}_i| = 1$) are the corresponding eigenvectors. Equation (1) denotes that signal change near a voxel center can be approximated by the sum of quadratic functions. Therefore, at a voxel through which a tag-plane runs, the following conditions are expected to be satisfied: (1) $\lambda_1 > 0$, (2) $|\lambda_1|$ is much larger than $|\lambda_2|$ and $|\lambda_3|$, (3) $\mathbf{v}_1$ is almost parallel to the readout direction which is orthogonal to the initial tag-plane, and (4) the position $\mathbf{x}-(\nabla f \cdot \mathbf{v}_1)/\lambda_1 \cdot \mathbf{v}_1$, which is the nearest center point of the tag-plane, is inside the voxel. In this study, all voxels at which the above four conditions were satisfied were selected as tag voxels and their nearest center points were detected as lying on tag-planes.

3 Results

Figure 2 shows cross-sectional images of typical LA images, which were reconstructed with five different ranges of respiratory levels, 100, 89, 57, 38 and 22%. The ranges are named ''R1'' to ''R5'', respectively. In spite of low temporal resolution (about 100 ms intervals), good tag-contrast is maintained during a whole cardiac cycle. Although the spatial resolution is different along the three directions (highest in the readout direction and very low in the other two), not only tag-contrast but also organ edges are clearly observed.

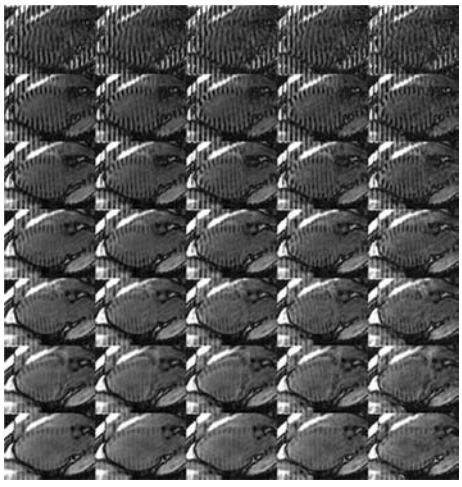

Fig. 2 Cross-sectional images of typical LA images which were reconstructed with different ranges of respiratory level, R1 to R5 (see text in detail). Digits assigned on the left column images represent cardiac phases from the R-wave trigger

Figure 3 shows cross-sectional images of detected tag-planes fused onto original SA1 and SA2 images. Almost all tag-planes observed on the original images can be detected well with our method. In particular, straight tag-lines detected on images taken at the first cardiac phase demonstrate that initial artifacts can be suppressed enough not to affect the tag-plane detection. Note that although detected tag-planes are displayed as aligned voxels, the center of the tag-lines can be estimated with subvoxel resolution.

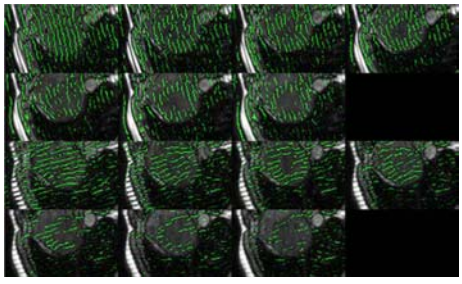

Fig. 3 Detected tag-lines fused on orginal SA1 (upper) and SA2 (lower) images

4 Conclusion

A four-dimensional MR tagged imaging method combined with retrospective respiratory gating, and an automatic tag-detection method based on a regional quadratic approximation technique, were developed. Resulting images show that clear tag-contrast is maintained during a whole cardiac cycle, and the tag-planes which are observed on the images can be well-detected with the proposed method.

In the future, real-time respiratory gating and optimum ''reordering'' (order of line-data acquisition in a k-space) will be introduced to shorten the total imaging time. For tagged image analysis, additional algorithms, such as deformable model based ones and/or manual corrections, are necessary to estimate tag-plane positions which have disappeared from the images or to eliminate detected points which are artifacts or on tag-plane locations not within the LV wall.

References

1. Zerhouni EA, Parish DM, Rogers WJ, Yang A, Shapiro EP (1988) Human heart: tagging with MR imaging: a method for non-invasive assessment of myocardial motion. Radiology 169:59–63
2. Axel L, Dougherty L (1989) Heart wall motion: improved method of spatial modulation of magnetization for MR imaging. Radiology 172:349–350

3. O'Dell WG et al (1995) Three-dimensional myocardial deformations: calculation with displacement field fitting to tagged MR images. Radiology 195(3):829–835
4. Schar M, Kozerke S, Fischer SE, Boesiger P (2004) Cardiac SSFP imaging at 3 Tesla. Magn Reson Med 51(4):799–806
5. Urayama S, Axel L, Okamoto J, Azuma T, Hanakawa T, Sugimoto N et al (2004) Transient artifact reduction with dispersion of phase (TARD) in coherent SSFP imaging. In: Proceedings of 90th RSNA, Chicago, USA, p 452
6. Deshpande VS, Chung YC, Zhang Q, Shea SM, Li D (2003) Reduction of transient signal oscillations in true-FISP using a linear flip angle series magnetization preparation. Magn Reson Med 49:151–157

Model creation strategies for segmentation of cardiac region in CT images

K.S. Shriram · M.J. More · S. Suryanarayanan
Imaging Technologies, GE Global Research, Bangalore, India

Abstract Model-based segmentation techniques using shape/texture priors are attractive solutions for cardiac segmentation owing to large variations in intensity and anatomy among subjects In this paper, we have compared the performance of three previously known model selection strategies for automated image-based segmentation of cardiac region. Additionally, we have introduced a novel model creation strategy that depends on the demographic profile of the target data. The models were created from a set of cardiac CT cases manually segmented by an expert. Each model was registered to a bank of target CT data and the extent of its agreement with the ground truth was used as the performance criteria. Finally, the model that demonstrated the best performance was selected for segmenting the normal cardiac CT and the saline flush CT acquisitions.

Keywords Segmentation · Model · Cardiac CT · Saline flush

1 Introduction

Segmentation of the heart and its chambers is a pre-requisite for 3-D visualization and quantitative functional analysis of cardiac CT. Heart segmentation is challenging due to the heterogeneity in anatomy and contrast variability from case to case as well as within chambers of the same case. Variations in scan/contrast timing, unpredictability of patient metabolism and new acquisition protocols such as the saline flush [1] further complicate the task, making intensity-based segmentation tools unreliable. Thus, there is a need for segmentation schemes that incorporate some higher-level anatomical information in the form of a model.

Prior attempts at model-based segmentation have taken two distinct approaches – statistical and non-statistical. Non-statistical approaches like Metaxas et al. [2] tend to approximate the region of interest in terms of geometric primitives such as ellipsoids and super-quadrics. In statistical approaches, Frangi et al. [3] have incorporated the shape information from a set of training cases into an automatically constructed point distribution model represented using an average shape along with the primary variation modes. Park et al. [4] create a probabilistic atlas of organs in the abdominal area where every voxel has an associated probability of belonging to a particular organ. However, the model selection process itself has not received a lot of attention. Rohlfing et al. [5] have studied four different atlas selection methods for segmenting confocal microscopy images of bee brains.

Our approach is along the lines of [5] but in the context of cardiac CT where the challenges are drastically different. We have introduced a novel model selection strategy where the choice of the model is conditional on the demographic profile of the data to be operated upon. Additionally, we compare this population-based model against three methods proposed in [5] namely, random selection (baseline), average model, and ''Best-case'' model. Models are compared against each other using ground truth obtained via expert segmentation of the heart.

2 Methods

2.1 Model creation

From a database of about 100 cases, a subset of 19 cases was chosen for training and subsequent testing. Variables such as gender, age, axial coverage, ethnicity, cardiac phase of acquisition, and field of view were considered during the down-selection. The 19 cases were further sub-divided into 10 training cases to build the model and 9 testing cases for performance analysis. The heart and the chambers were manually segmented by two radiologists using an existing software tool. Each expert segmented 30 cases, 10 of which were overlapped with the other expert to quantify the inter-reader variability. The extent of agreement between the two operators was measured using the Dice Similarity Coefficient (DSC), defined as:

$$\mathrm{DSC} = \frac{2\left(\mathrm{Vol}_{\mathrm{op1}} \cap \mathrm{Vol}_{\mathrm{op2}}\right)}{\left(\mathrm{Vol}_{\mathrm{op1}} \cup \mathrm{Vol}_{\mathrm{op2}}\right)}$$

where, $\mathrm{Vol}_{\mathrm{op1}}$ and $\mathrm{Vol}_{\mathrm{op2}}$ are the volumes carved out by operators 1 and 2 respectively.

2.2 Model selection strategies

Random model This scheme forms the baseline for all the other methods, is unbiased and a starting point in all the other studies. It involves picking a random case from the training database and designating it as the model.

Best-case model The aim here is to select a case as the model that best represents the average shape of the population. This is the central representative of the training cluster and hence, undergoes the least amount of deformation while matching to a target case. All the n images in the training database are co-registered with each other and the overlaps are calculated creating an $n \times$ n matrix of the DSC values. For a specific case p chosen as the model, the performance measure is computed as:

$$\mu_{\mathrm{DSC}} = \frac{\sum_{i=1}^{n} \mathrm{DSC}(i,p)}{n};$$

$$\sigma_{\mathrm{DSC}} = \sqrt{\frac{1}{n}\sum_{i=1}^{n}\left(\mathrm{DSC}(i,p) - \mu_{\mathrm{DSC}}\right)^2}; \quad \mathrm{COV} = \frac{\mu_{\mathrm{DSC}}}{\sigma_{\mathrm{DSC}}}$$

The case that is most central in the cluster i.e. having the highest coefficient of variance (COV) for DSC values is picked as the best-case model. Park et al. [6] in their implementation have used a matrix of the bending energies of all the registration pairs, picking the case that lies around the mean as the best-case model.

Average model Here, all the segmented volumes from the training set are aligned together and averaged (either by simple averaging of intensities or by majority voting), forming the averaged model. In iterative averaging [7], a random case from the training database is chosen as the seed, to which all the other cases are registered. The intensities are then averaged; the average now becomes the seed to which all the training cases are registered in the subsequent iteration. This process is repeated until convergence.

Iterative averaging scheme faces challenges while dealing with heterogeneous data exhibiting large variations like cardiac CT, where mis-registrations at the periphery might lead to averaging intensities from disparate regions. To overcome the problems associated with large-scale deformations, Lorenzen et al. [8] have proposed a diffeomorphism-based approach for creating a population average.

Population-based model The idea behind this scheme is to pick the model from the training database that is closest to the target data in terms of demographic profile. We studied age and gender as the possible demographic categories while holding ethnicity and CT acquisition parameters constant. Volumes were measured from the segmented hearts obtained from the experts. We found that while there is a significant difference in heart volumes between male and female cases, the relationship between heart volumes and age profile remained inconclusive. The training dataset was divided into male and female subgroups and the cases closest to the average heart volume in both the clusters were picked as the population-based

models. The implementation of this scheme involves obtaining the gender information of the target case from the DICOM header and matching it with the corresponding model.

2.3 Registration framework

To capture statistical variation, each of the training datasets has to be aligned to a common coordinate frame using a registration algorithm. The basic components of the registration framework are two input images, a transform, a metric, an interpolator and an optimizer. Global rigid registration with the target as the fixed image and the model as the moving image was implemented using the Insight Tool Kit [9].

Transform The Affine and the Versor transforms were considered for experimentation. The rotation/scaling/shear coefficients accompanying the transform are usually of a very different dynamic range compared to translation. In the case of our cardiac CT database, the dominant transform required to register images was translation, accompanied by small amounts of rotation/scaling/shear.

Metric The choice of metric was between Mutual Information (MI) and Mean Square error (MSE). MSE makes eminent sense for intra-modality registration, while MI has a more generic framework suitable even for inter-modality registration.

3 Results

3.1 Manual segmentation

The segmented output from both operators was found to be in good agreement with each other. The average DSC over the ten overlapping cases was calculated to be 96% (σ = 1.3%).

3.2 Registration framework

To compare similarity metrics, five manually segmented cases were co-registered with each other and DSC comparison with the ground truth was used for evaluation. It was found that both MI and MSE metrics resulted in similar accuracies (Fig. 1a) with the only difference being that MI required significantly less time for computation. MI being more statistical in nature works even if the images are sampled sparsely for computing the joint histograms. Similarly, affine and versor transforms were evaluated using three manually segmented cases and DSC was used for comparison. The accuracies with both affine and versor were comparable (Fig. 1b), the difference being the versor transform was found to be more stable across all the registration pairs. Figure 1b shows a case (50_10) where the affine transform failed to produce any results. Thus, versor transform with MI metric was used for all further model to target registrations.

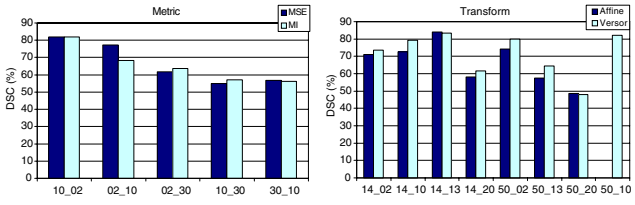

Fig. 1 Comparison of overlaps with ground truth of: **a** *left* MI and MSE metrics and **b** *right* affine and versor transform when used to drive registration

3.3 Model selection

Best-case model Table 1 shows the 10 × 10 matrix of DSC values along with the COV for each of the training cases. Higher the COV, better the model at representing the population. In our case, CT_46 (Table 1) was picked as the Best-case model.

Average model Simple averaging after co-registration of training images could not handle large spatial and intensity variations in the heart chambers. When all the training images were co-registered to a common coordinate frame, the overlaps among the chambers of the heart were not high enough to mandate a probabilistic atlas (Fig. 2); hence the average model was discarded.

Population-based model The training dataset was divided into two clusters based on gender. The efficacy of this method was tested by comparing situations where model and target were of the same gender (intra category) to one where they belonged to different ones (inter category). We found that female–female transformations performed better than female–male transformations, while difference between male inter- and intra-category transformations was not conclusive. A two sample *t*-test yielded a *P*-value of 0.18 indicating that the difference between the inter- and intra-category registration was not significant. This result could be due to the limited nature of the training database.

Table 1 The 10 × 10 matrix of DSC values generated by co-registering all the training cases with each other. Moving image was taken as the model while the fixed image as the target. CT_46 was chosen as the Best-case model since it had the highest COV

Target	Model									
	CT_02	CT_10	CT_13	CT_14	CT_18	CT_19	CT_20	CT_43	**CT_46**	CT_50
CT_02		88	83	94	89	85	78	90	**91**	91
CT_10	85		84	90	87	88	83	92	**92**	93
CT_13	89	88		91	88	87	81	91	**90**	88
CT_14	95	91	91		92	91	77	94	**93**	91
CT_18	90	91	90	92		89	77	77	**92**	90
CT_19	91	92	86	93	89		64	92	**94**	93
CT_20	71	75	88	76	89	71		60	**87**	81
CT_43	86	84	71	86	77	80	69		**87**	89
CT_46	90	88	86	91	84	87	80	92		91
CT_50	82	87	81	82	85	88	70	89	**85**	
AVG_DSC	86	87	84	88	87	85	75	86	**90**	90
Stdev_DSC	7	5	6	6	4	6	6	11	**3**	4
COV	12.54	16.41	14.23	14.64	20.17	13.73	12.13	7.96	**29.86**	25.00

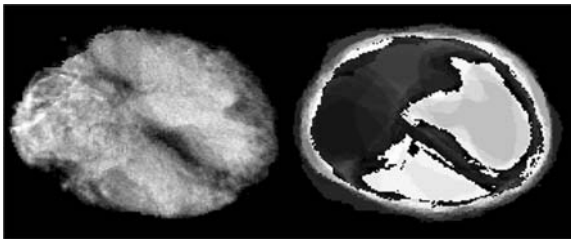

Fig. 2 Average model obtained by averaging intensities (*left*); overlap between the individual chambers (*right*). Misalignment is greater in the atria than in the ventricles

The performance of the Random, Best-case and the Population-based models were compared (in terms of DSC) on the training examples. The Best-case model was found to outperform the other two with an average DSC of 90.4% across all cases (σ = 3%). The comparative study was further validated on the test cases and similar results were obtained. Figure 3 (top) shows an example where the Best-case model was registered to a test CT case. Finally, the Best-case model was implemented on Saline flush data whose right chambers were devoid of any contrast. Figure 3 (bottom) shows that the model aligned well with the target heart in its entirety notwithstanding the vagaries of the intensity values on the right side chamber of the target. After accurate alignment, the model was used as a mask to segment the heart from the target CT image. The volume rendered image of the segmented heart for a saline flush target case is shown in Fig. 4 (bottom) and compared against that obtained from a bottom-up method (top).

4 Conclusions

In this paper we have studied four model creation strategies for cardiac CT, including a novel strategy based on the demographic profile of the target data. Using an ITK-based registration framework we selected MI over MSE for the choice of similarity metric and the versor transform over the affine transform for our application. The

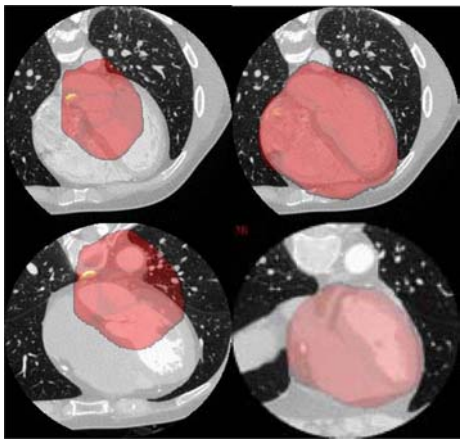

Fig. 3 Best-case model overlaid on the target CT image before (*left*) and after (*right*) registration. The *top row* shows model registration to target for a normal CT acquisition while the *bottom row* is for a saline flush case

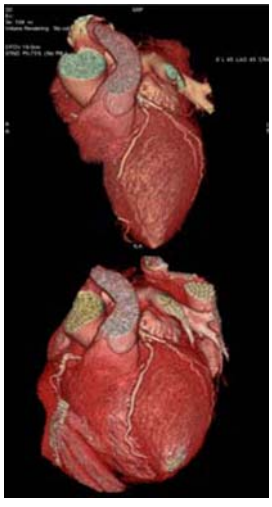

Fig. 4 Heart Segmentation for a saline flush case using bottom-up method (*top*) versus model-based method (*bottom*)

Best-case model outperformed the Random and the Average models. The Average model based purely on global registration gave anatomically unacceptable output owing to the large variations in the individual chambers. The Population-based model did not perform significantly better perhaps because of the limited datasets used in our study. Finally, we demonstrated segmentation of cardiac region from saline flush cases that present a big challenge in the form of inter-chamber contrast variability.

Acknowledgements The authors would like to thank the team of radiologists from Teleradiologiy Solutions, India for their help in creating manual cardiac models and Dr. Rakesh Mullick (GE Global Research) for his assistance with the registration framework.

References

1. Lawler LP (2004) Coronary CT angiography. Online Supplement to Applied Radiology
2. Metaxas D, Chen T, Huang X, Axel L (2004) Cardiac segmentation from MRI-tagged and CT images. In: Proceedings 8th WSEAS international conference on computers
3. Frangi AF, Rueckert D, Schnabel JA, Niessen WJ (2002) Automatic construction of multiple-object three-dimensional statistical shape models: application to cardiac modeling. IEEE Trans Med Imaging 21(9):1151–1166
4. Park H, Bland PH, Meyer CR (2003) Construction of an abdominal probabilistic atlas and its application in segmentation. IEEE Trans Med Imaging 22(4):483–492
5. Rohlfing T, Brandt R, Menzel R, Maurer CR (2004) Evaluation of atlas selection strategies for atlas-based image segmentation with application to confocal microscopy images of bee brains. NeuroImage 21:1428–1442
6. Park H, Bland PH, Hero AO, Meyer CR (2005) Least biased target selection in probabilistic atlas construction. In: Proceedings of MICCAI
7. Rohlfing T, Brandt R, Maurer CR, Menzel R (2001) Bee brains, B-splines and computational democracy: generating an average shape atlas. IEEE workshop on mathematical methods in biomedical image analysis, IEEE Computer Society, Los Alamitos, CA, pp 187–194, Kauai
8. Lorenzen P, Davis B, Joshi S (2005) Unbiased atlas formation via large deformations metric mapping. In: Proceedings of MICCAI
9. Ibanez L, Schroeder W, Ng L, Cates J, The Insight Software Consortium, The ITK Software Guide, 2nd edn. Updated for ITK version 2.4, http://www.itk.org

A versatile tool for flow analysis in 3D-phase-contrast magnetic resonance imaging

R. Unterhinninghofen[a] · S. Ley[b,d] · J. Zaporozhan[b] · G. Szabó[c] · R. Dillmann[a]

[a]Institute of Computer Science and Engineering, University of Karlsruhe, Germany

[b]Department of Radiology, German Cancer Research Centre Heidelberg, Germany

[c]Department of Cardiac Surgery, University Hospital Heidelberg, Germany

[d]Department of Pediatric Radiology, Children's University Hospital Heidelberg, Germany

Abstract Phase-Contrast Magnetic Resonance Imaging (PC-MRI) is a technique that allows radiologists to non-invasively assess blood flow While its routine use is limited to the quantification of flow in vessels based on one-dimensional velocity-encoded images, more recent sequences allow for the acquisition of complete velocity vector fields in a reasonable setting. These vector fields may give a deeper insight into the physiological or patho-physiological conditions in large vessels such as the aorta. Currently clinicians lack appropriate software tools that combine classical flow visualization with medical image processing. In this paper we present a dedicated, versatile software tool for the analysis of 3D-PC-MRI flow data, which is based on the MEDIFRAME application framework. It implements several visualization and quantification techniques including virtual echocardiography and streamlines. Examples from animal experiments illustrate its usage and usefulness.

Keywords MRI, Vascular imaging · Flow visualization · Flow quantification

1 Introduction

Phase-Contrast Magnetic Resonance Imaging (PC-MRI) is a technique that allows radiologists to non-invasively assess blood flow by measuring local blood velocities. It is based on the fact that nuclear spins, when moving along a magnetic gradient, get a phase shift proportional to their velocity. This implies that velocity measurement is possible only along one user defined axis. However, more recent imaging sequences acquire such flow-sensitive images along three orthogonal axes in rapid succession that the result may be taken as three-dimensional velocity vectors.

Conventional, i.e. one-dimensional PC-MRI is often used to measure flow, particularly in large vessels such as the aorta or the pulmonary artery [1, 2]. Commercially available software tools, e.g. ARGUS (Siemens Medical, Erlangen, Germany) compute the effective blood flow through a manually defined region of interest. 3D-velocity-encoded phase images, on the other hand, are generally difficult to

interpret visually and currently there is virtually no commonly accepted application in the radiological practice. Moreover, the lack of appropriate software tools impedes the exploitation of the velocity vector data in the clinical routine.

This technique does not only deliver quantitative information about blood flow, it can also give valuable insight into specific pathological flow patterns. For example it may be possible to track regurgitational flow through insufficient heart valves or to examine the main direction of flow in large vessels.

In this paper we present a new versatile software tool that is dedicated to analyze vectorized flow data acquired using 3D-PC-MRI and we illustrate its usage with a few examples from animal experiments.

2 Methods

2.1 Data

For this work a 3D phase-contrast sequence has been used on a Siemens Magnetom Symphony 1.5 T MR-Scanner. It is based on the FLASH sequence and allows the acquisition of a time-resolved field of three-dimensional blood velocity vectors on one two-dimensional slice – in addition to the morphological image. The sequence is ECG-triggered. Several parallel, 5 mm thick slices are acquired consecutively at equidistant positions, resulting in two datasets: morphology and velocity field (see Fig. 1). Technically, both are discrete regular 4D grids (x,y,z,t) with 1D (morphology) and 3D (velocity vectors) data defined on it. The size of the datasets usually adds up to 150 MB.

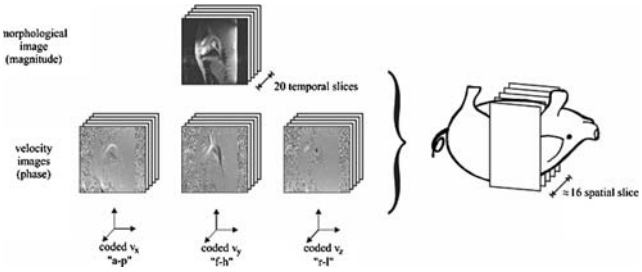

Fig. 1 MRI acquisition scheme

A series of animal experiments have been used to test the software tool. In ten domestic pigs sagital slices of the heart and the aorta were acquired on a 256×256 pixels matrix. Voxel size was $1.4 \times 1.4 \times 5$ mm^3, VENC was set at 100 cm/s. The acquisition was performed without any breath-hold using retrospective ECG-triggering.

2.2 Software tool

MEDIFRAME is an extendable software framework for medical applications that has been developed at the Institute of Computer Science and Engineering, University of Karlsruhe [3]. Apart from being a high-level application framework it offers basic functionality needed for medical applications such as volume and sliced visualization of image data, DICOM import and data management. It has been implemented in C++ and is available for all common platforms (Windows, Linux and MacOS). A flexible plug-in concept allows for easy integration of application-specific components.

The tool for the analysis of vector flow data, which is being presented here, has also been realized as a plug-in component. At startup the user may select morphological and corresponding velocity encoded data into the component.

The component basically offers three different ways to visualize the data: virtual echocardiography, vector flow and streamlines. In any case the morphological data is rendered as a three-dimensional volume using VTK raycasting (The Visualization Toolkit, Kitware, New York, USA). Hardware accelerated raycasting using VolumePro (Terarecon, San Mateo, USA) is also supported and quite advantageous for the large datasets. Additionally the data may be viewed in up to three arbitrary cross-section planes. The complete representation may be animated playing the whole heart cycle as a video.

2.3 Visualization techniques

Virtual echocardiography is a visualization technique that emulates in some way the Color-Doppler Echocardiography which is well known to medical doctors. A virtual transducer is displayed on the screen and may be placed and oriented arbitrarily [4, 5]. Consequently the flow data is blended with the morphological data with blood moving towards the transducer being colored red and blood moving away from the transducer being colored blue. Of course, movement in a perpendicular direction is not visible at all. Although this method seems to go against the idea of vector field visualization it turned out to be a good way to interactively explore the flow.

Vector flow visualization is the most common way to represent flow: small arrows show the direction of the velocity vectors at each position. However, with the 3D data at hand, this technique must be appropriately adapted to be useful. For example it would be not helpful to display an arrow at every voxel because due to the sheer number of arrows it would be impossible to get any useful information. Hence a probing technique has been implemented, i.e. the vector arrows are only displayed at certain probing points. The user may for example define a plane with equally distributed probing points and move it through the data.

Streamlines are also a well known method to visualize flow. Streamlines allow tracking the way a particle takes through the velocity field. In this tool the user may define the starting points for streamlines and observe the traces.

In order to complete the functionality, the tool also offers the possibility to quantify flow through arbitrary elliptical planes. The user may place an elliptical plane for example into a vessel and fit it to the vessel wall. The software automatically computes the flow and the effective stroke volume over the whole heart cycle, where the specific placement of the elliptical plane may be adjusted for each time frame. Technically, the vector field is projected to the normal of the plane and integrated over the defined area. The results are displayed as a bar graph and a numerical table. Additionally the flow profile of the region of interest may be viewed.

3 Results

Visualization of vector fields is generally known to be difficult because of the high-dimensional nature of the data. The techniques presented above all aim to reduce the data in some way, which makes it cognizable, but which also brings along the need for interactive exploration, i.e. changing the view in order to find and to collect the needed information.

The software tool proved to be sufficiently fast for this purpose thanks to optimized multi-threaded programming. Also, the flexibility, i.e. the possibility to combine or quickly change the different visualization functions showed to be very useful. However, the three-dimensional visualization of vector arrows and streamlines in combination with raycasted morphology was not yet optimal as under certain view angles the arrows did not appear at the right depth, i.e. they seemed to lie outside the volume. This is due to problems of blending raycasted images and polygonal surface-mesh data, especially when using VolumePro.

The software has been tested with different datasets. The visualization of large flow patterns such as aortic or pulmonary outflow or left-ventricular diastolic inflow was easily possible and showed to be quite instructive. Also ventricle vortexes were observed (Figs. 2, 3).

4 Conclusion

While phase-contrast magnetic resonance imaging is mainly used for the quantification of flow in vessels today, its capabilities to acquire three-dimensional velocity fields remain unused in the radiological routine. We presented a software tool to process and visualize velocity field data from MRI giving insight into the flow characteristics of a specific patient. The tool showed to be functional and useful. However, more work needs to be done concerning usability and more adapted views, e.g. more specialized probing schemes.

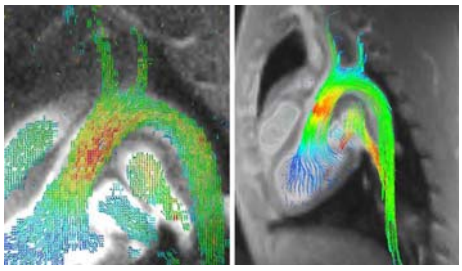

Fig. 2 Flow visualization in the aortic arc using vector arrows (*left*) and streamlines (*right*). *Color* corresponds to velocity magnitude

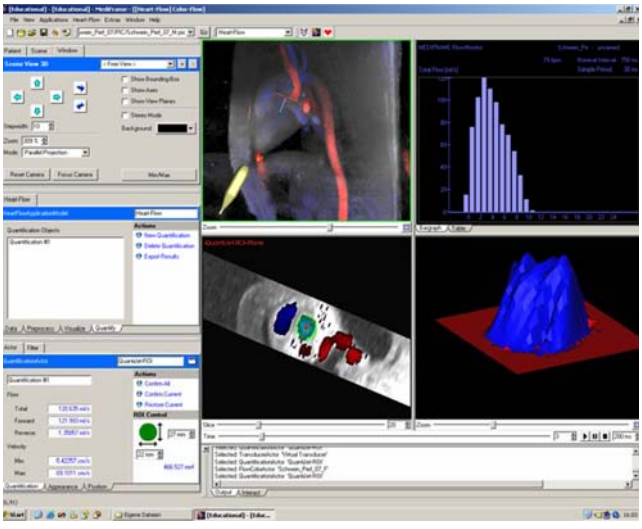

Fig. 3 Flow quantification: elliptical plane placed in the ascending aorta (*upper left*: 3D virtual echocardiography, *lower left*: cross-sectional view, *upper right*: flow over time, lower right: flow profile)

Currently the accuracy of the quantification function is examined. Furthermore specific segmentation techniques are being implemented in order to help the user track interesting flow more easily.

References

1. Powell AJ, Geva T (2000) Blood flow measurement by magnetic resonance imaging in congenital heart disease. Pediatr Cardiol 21:47–58
2. Zhang H, Halliburton SS, Moore JR, Simonetti OP, Schvartzman PR, White RD, Chatzimavroudis GP (2002) Accurate quantification of steady and pulsatile flow with segmented k-space magnetic resonance velocimetry. Exp Fluids 33:458–463
3. Seifert S, Burgert O, Dillmann R (2002) MEDIFRAME – An extendable software framework for medical applications. Surgetica 2002, Grenoble, France
4. Unterhinninghofen R, Albers J, Hosch W, Vahl CF, Dillmann R (2005) Multidimensional interactive colour-coding in velocity encoded magnetic resonance images of mitral insufficiency, Surgetica 2005, Chambéry, France
5. Nayak KS, Hu BS (2003) Triggered real-time MRI and cardiac applications. Magn Reson Med 49:188–192

Nonrigid registration for subtraction CT angiography applied to the carotids and cranial arteries

D. Loeckx[a] · F. Maes[a] · D. Vandermeulen[a] · P. Suetens[a] · W. Coudyzer[b] · G. Marchal[b] · G. Wilms[b]

[a]Medical Image Computing (PSI), Department of Electrical Engineering, Faculty of Engineering, Katholieke Universiteit Leuven, Belgium

[b]Radiology Section, Department of Medical Diagnostic Sciences, Faculty of Medicine, Katholieke Universiteit Leuven, Belgium

Abstract Computed tomography angiography (CTA) is an established tool for vascular imaging However, high-intense nonvascular structures in the contrast image can seriously hamper luminal visualisation. Even when using subtraction CTA, where a native image is subtracted from the contrast image, patient and organ motion limits the widespread application of this technique. Within this paper, a procedure is presented to overcome this problem. First, a native image without contrast administration and a contrast image after contrast administration are acquired. Next, the images are transmitted to an image processing workstation. In this workstation, the native image is registered to the contrast image using an automatic intensity-based nonrigid three-dimensional registration algorithm. The registered native image and the contrast image are fused to create the arterial and bone image. Finally, the newly created images are send back to the console for visualisation. Our method allows the user to switch between a view of the arteries, the bone or both. The average calculation time of the whole procedure is about 30 min. This procedure has been used to image the carotids of 31 patients. Although the patients were carefully instructed not to move between the two scans, and exactly the same region was imaged, all initial data sets show significant movement artifacts. In all cases, the artifacts are reduced by the nonrigid registration. Remaining artifacts mostly occur in the tooth region, well separated from the vessels of interest.

Keywords CTA, CT angiography · sCTA · Subtraction CT angiography · Head-and-neck · Parotids · Registration

1 Purpose

With the ever increasing temporal and spatial resolution of multidetector CT scanners, CT has become an excellent modality for accurate imaging of vascular structures. Therefore, CT angiography (CTA) is since some years used in daily clinical practice [1]. Especially in combination with volume rendering, CTA images often are a helpful clinical tool. Nevertheless, when the blood vessels of interest, which appear high-intense on the contrast-enhanced images, are located near other high-intense structures like bone or plaques, intensity thresholding or volume rendering is not suitable to discriminate the vessels. In those cases, registration of pre- and post-contrast images and subsequent subtraction of the co-registered images provides an elegant solution. Several authors published promising work using a rigid registration approach (e.g. [2]). However, due to subtle changes in pose or muscle tension, rigid registration is often insufficient to cover all changes and nonrigid registration is often required.

A region that is especially of interest for subtraction CTA is the head-and-neck region. Precise noninvasive evaluation of the cervicocranial vessels is of utmost clinical importance. The main diagnostic issues concern the demonstration of the presence and degree of stenosis of the cervical vessels and of concomitant lesions of the intracranial vasculature. Detection and quantification of stenoses of the cervical arteries appears very accurate with CTA, allowing application of the NASCET-criteria [3, 4]. For the intracranial vessels, besides the diagnosis of stenosis and occlusion, other diseases benefit from early and noninvasive diagnosis with CTA. In the diagnosis of intracerebral aneurysms the accuracy of CTA approaches 100% when compared with DSA [5, 6]. It can miss smaller aneurysms, inferior to 4 mm, but is superior as a fast noninvasive method without complications [7].

Bone subtraction seems to be useful to avoid superposition of bony structures especially in the vertebrobasilar system [8]. It furthermore might be important to allow determination of the degree of stenosis in heavily calcified plaques [9].

2 Methods

We have implemented a method that allows nonrigid 3D registration of the pre-contrast image to the post-contrast image in a clinically

acceptable time, using a standard PC workstation for the image processing part. The procedure consists of the following steps:

1. Acquire the native (pre-contrast) image
2. Administer contrast and record the contrast enhanced (post-contrast) image
3. Send both images to the image processing workstation
4. Nonrigidly register the native image to the contrast enhanced image
5. Fuse the registered images into a single dataset
6. Transmit the fused image back to the CT console
7. Visualise the images

The whole procedure is fully automated, thus requiring no user interaction.

2.1 Acquisition setup (steps 1–2)

All images are recorded on a Siemens Sensation 64 (Siemens, Erlangen, Germany) using 120 keV radiation at about 500 mA s and a pitch of 1.2. Reconstructed images contain 512×512 pixels and 700–900 slices with a cubic voxel size of about 0.4 mm $\times$ 0.4 mm $\times$ 0.4 mm. Care was taken that the contrast enhanced image is acquired with exactly the same settings (i.e. field of view, voxel size, reconstruction filter,...) as the native image. The patients were carefully instructed not to move between the two scans, and exactly the same acquisition settings were used. Recording takes about 30 s per scan with an interval of about 2 min between the scans to administer contrast.

2.2 Image registration (step 4)

The nonrigid deformation is modelled by a B-spline deformation mesh [10]. As similarity measure, mutual information between the native and contrast enhanced image is chosen [11]. A grid of mesh control points is positioned over the image. A multiresolution optimisation algorithm is adopted, using four multiresolution steps. Initially, to model a more global deformation, the grid spacing is large, yielding a coarse mesh with few control points. The final finer mesh has small grid spacing and many control points, allowing a more local deformation. In the first two steps, the images are downscaled three times in each direction (i.e. using only $1/8^3 = 1/512$ of the original voxels). In the last two steps, the images are downscaled twice with respect to the original image sampling. Initially, a mesh spacing of 128 voxels is used, gradually decreasing to 64 voxels in steps 2 and 3 and 32 voxels in the last step. As the registration algorithm has subvoxel precision; the obtained smaller scale deformation can be upscaled retaining sufficient accuracy [12]. The multiresolution approach greatly reduces calculation time by performing the initial calculations on a smaller image. Gradually decreasing the grid spacing will first recover more global deformations and progressively advance to finer deformations, thus creating a more realistic deformation field and avoiding local optima. After registration, the obtained transformation is applied to the full-scale original native image, yielding the deformed native image.

2.3 Image fusion (step 5)

On the basis of the intensities in the registered native and contrast enhanced image, each voxel is classified as bone (high intense in both images), vessel (high intense in the contrast enhanced image, low intense in the native image) or soft-tissue (low intense in both images). A fused image is created, in which soft tissue voxels are set to 0 HU (Hounsfield units), vessel intensities remain unchanged and bone voxel intensities are mirrored around 0 HU (i.e. the sign is inverted). This leads to a histogram in which the vessel voxels remain situated in the range around 300 HU, all soft tissue is concentrated at 0 HU and the bone voxel intensities are situated in the range −100 to −1,000 HU. Therefore, vessel and bone intensities are well separated and can be visualised independently.

2.4 Visualisation (step 7)

The images are visualised on the Siemens Syngo (Siemens, Erlangen, Germany) volume renderer. Due to the construction of the fused image, the normal volume rendering settings can be used to visualise the arteries. An extra ramp can be inserted for the bone voxels; its transparency can be individually controlled.

3 Validation

The registration quality is measured by the average intensity of the voxels with negative intensity in the subtraction image [13]. As the administered contrast causes an increased intensity in the contrast-enhanced image, corresponding voxel intensities in the contrast enhanced image are expected to be higher (in the vessels) or equal (everywhere else) to the voxel intensities in the native image. Negative intensities in the difference image ($I_{\text{contrast enhanced}} - I_{\text{native}}$) are caused by registration inaccuracy or CT acquisition artefacts. To visually asses the registration quality, error images are created showing the sum of the negative voxels in the difference images. Darker pixels reflect more artefacts and thus a worse registration; brighter pixels indicate no errors. The images give an indication of the location of the registration artefacts and a visual demonstration of the artefact reduction over increasing registration stages.

4 Results

The automated registration procedure has been used to image the carotids of 31 patients. Initially, all datasets show significant movement artefacts; the average negative error is 25.6 HU. This error gradually decreases over the registration stages to 9.9 HU in the final stage. This final error is comparable to the error due to normal multislice spiral CT artefacts [14]. An example of the results obtained without and with registration is shown in Fig. 1. When the bone is rendered completely transparent, a clear view of the vessels is generated. Figure 2 shows some details of the passage of the carotids through the skull base. Alteration of the bone transparency allows changing the visibility of the calcified structures, and thus also allows distinguishing between soft and hard plaques, as shown in Fig. 3. Figure 4 displays, for a typical patient, the error images for each registration stage. A clear reduction of registration artifacts can be seen; the remaining artifacts are mainly situated in the tooth region, well separated of the vessels of interest.

Fig. 1 Fused images, before (*left*) and after nonrigid registration (*middle and right*). In the middle image, the bone is shown semi-transparent, in the *left* and *right* image it is shown transparent. Due to misregistration, most of the skull is visible in the left images and e.g. the left clavicle

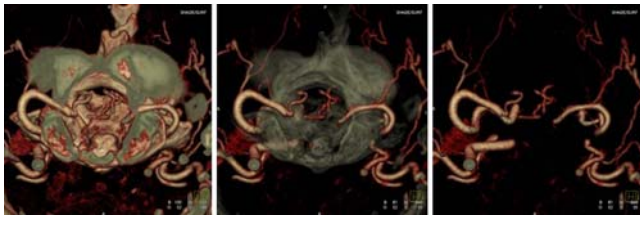

Fig. 2 Detail of the passage of the carotids through the skull base, original contrast image (*left*), with semi-transparent bone (*middle*) and with transparent bone (*right*)

The average processing time per patient is about 30 min on a Dell PowerEdge 2600, requiring about 20 min for the registration.

5 Conclusion

In this paper, we presented a nonrigid registration algorithm that substantially reduces the movement artefacts in subtraction CT angiography, allowing for a clear 3D view of the vascular structure.

Fig. 3 Detail of the carotid bifurcation, (*left*) original contrast image, (*middle*) with semi-transparent bone and (*right*) with transparent bone. The left stenosis is caused by soft plaque, visible in none of the images. The right stenosis is caused by hard plaque, visible in the original image, semi-transparant in the middle image and invisible in the right image

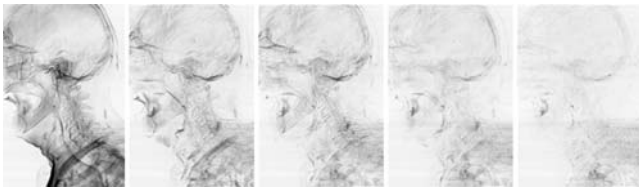

Fig. 4 Axial view of error images from left to right without registration and for stage 1, 2, 3 and 4. The images give an indication of the location of the registration artefacts and a visual demonstration of the artefact reduction with ongoing registration stages. Window/level is kept fixed for all images

The algorithm was successfully tested on 31 datasets. The method is fully automated and runs in the background. The method has the potential to enable e.g. accurate diagnosis of emergency patients with stroke indications in less than an hour, allowing for a much quicker and thus better treatment, which is subject of future work.

Acknowledgements This work is supported by the K.U.Leuven (project/OF/GOA/2004/05) and by the Fund for Scientific Research–Flanders (FWO-Vlaanderen, project FWO/G.0258.02 and FWO/G.0566.06).

References

1. Rankin SC (1998) Spiral CT: vascular applications. Eur J Radiol 28:18–29
2. Kwon S, Kim Y, Kim T, Ra J (2004) Digital subtraction CT angiography based on efficient 3D registration and refinement. Comput Med Imaging Graph 28:391–400
3. Bartlett ES, Walters TD, Symons SP, Fox AJ (2006) Quantification of carotid stenosis on CT angiography. AJNR Am J Neuroradiol 27:13–19
4. Josephson SA, Bryant SO, Mak HK, Johnston SC, Dillon WP, Smith WS (2004) Evaluation of carotid stenosis using CT angiography in the initial evaluation of stroke and TIA. Neurology 63(3):457–460
5. Tomandl BF, Hammen T, Klotz E, Ditt H, Stemper B, Lell M (2006) Bone-subtraction CT angiography for the evaluation of intracranial aneurysms. AJNR Am J Neuroradiol 27:55–59
6. Goddard AJ, Tan G, Becker J (2005) Computed tomography angiography for the detection and characterization of intra-cranial aneurysms: current status. Clin Radiol 60(12):1221–1236
7. Kangasniemi M, Makela T, Koskinen S, Porras M, Poussa K, Hernesniemi J (2004) Detection of intracranial aneurysms with two-dimensional and three-dimensional multislice helical computed tomographic angiography. Neurosurgery 54(2):336–340; discussion 340–341
8. Lell M, Anders K, Klotz E, Ditt H, Bautz W, Tomandl BF (2005) Clinical evaluation of bone-subtraction CT angiography (BSCTA) in head and neck imaging. Eur Radiol 1–9 [Epub ahead of print]
9. McKinney AM, Casey SO, Teksam M et al (2005) Carotid bifurcation calcium and correlation with percent stenosis of the internal carotid artery on CT angiography, Neuroradiology 47(1):1–9 [Epub 2005 Jan 14]
10. Loeckx D, Maes F, Vandermeulen D, Suetens P (2004) Nonrigid image registration using free-form deformations with a local rigidity constraint, MICCAI 2004, pp 639–646
11. Maes F, Collignon A, Vandermeulen D, Marchal G, Suetens P (1997) Multimodality image registration by maximization of mutual information. IEEE Trans. Med. Imaging 16(2):187–198
12. Loeckx D, Maes F, Vandermeulen D, Suetens P (2006) Comparison between Parzen window interpolation and generalised partial volume estimation for non-rigid image registration using mutual information, WBIR 2006 (in press)
13. Loeckx D, Drisis S, Maes F, Vandermeulen D, Marchal G, Suetens P (2005) Removal of plaque and stent artifacts in subtraction CT angiography using nonrigid registration and a volume penalty, MICCAI, pp 361–368
14. van Straten M, Venema HW, Hartman J, den Heeten GJ, Grimbergen CA (2004) Reproducibility of multi-slice spiral computed tomography scans: an experimental study. Med Phys 31(10):2785–2786

Automatic prediction of infarct growth in acute ischemic stroke from MR apparent diffusion coefficient maps

N. Hevia Montiel[a] · C. Rosso[a,b] · M. Chupin[a] · S. Deltour[b] · E. Bardinet[a] · D. Dormont[a,c] · Y. Samson[b] · S. Baillet[a]

[a]Cognitive Neuroscience & Brain Imaging Laboratory, CNRS UPR640-LENA; AP-HP, La Salpêtrière Hospital; Pierre & Marie Curie University, Paris, France

[b]AP-HP; Brain Stroke Emergency Unit, La Salpêtrière Hospital, Paris, France

[c]AP-HP; Neuroradiology Department, La Salpêtrière Hospital, Paris, France

Abstract We introduce a new approach to the prediction of the final infarct growth in human acute ischemic stroke based on image analysis of the apparent diffusion coefficient (ADC) MR maps acquired in the acute stage The ADC maps are likely to reveal brain regions belonging to the ischemic penumbra, that is, areas that may be affected by the infarction in the following next few hours. In a context where ''time is brain'', and contrarily to the most developed—though still-debated—perfusion–diffusion mismatch approach, the ADC MR sequences are fast to acquire and do not necessitate injection of a contrast agent. Image analysis consists of the segmentation of the ischemic penumbra using a fast 3D region-growing infarct approach.

Keywords Stroke · Magnetic resonance imaging · Diffusion imaging · Region-growing segmentation · Cerebral ischemia · Infarct growth prediction · Apparent diffusion coefficient

1 Introduction

In the immediate aftermath of acute ischemic stroke, knowledge on the significant growth potential of radiological abnormalities detected during the early therapeutic window is of critical importance. Prediction of the regions—and consequently functional systems—eventually involved in the infarct will influence the very choice of the most effective therapy. In this context, recent MR sequences could contribute to reduce the huge social impact of stroke if image analysis tools for accurate and immediate distinction between the already-infarcted and still-at-risk ischemic tissues can be provided. A first approach consists in determining thresholds on imaging measures to distinguish between regions (1) bound to spontaneous recovery, (2) threatened but potentially viable, the ischemic penumbra or, (3) irreversibly injured and infarcted [12]. The penumbra region is an assembly of areas that may be affected by the infarction in the following next few hours. It includes functionally impaired but

salvageable ischemic brain tissue surrounding an irreversibly damaged core.

Like in other non-ischemic CNS pathologies, basic structural MRI can help reveal the earliest hemodynamic and a tissue change induced by ischemia [4], but carries no information about the forthcoming outcome of the infarct growth. In this context, the perfusion–diffusion mismatch approach has been proposed to estimate the growth potential of the infarct in the acute phase, with limited specificity though [1, 11]. Alternatives based on diffusion MR imaging such as diffusion-weighted (DWI) and apparent diffusion coefficient (ADC) maps may unveil three types of information: the initial location of the early cerebral ischemic accident; the final volume of abnormalities with irreversible lesions at the time the MRI scan was acquired; and the severity of ischemia. Because of the advent of these techniques in clinical MRI units, recent studies have highlighted the clinical value of DWI in stroke diagnosis and the potential impact of water ADC measurement on the quantification and prediction of histopathologic damage in ischemic brain infarcts [7, 8, 9]. DWI for instance, reveals relative hypersignals in regions with lower diffusion, such as areas of acute stroke. Tissues in which water diffusion is reduced can therefore be readily detected as a hyperintense area on heavily diffusion-weighted MR images, which has become the hallmark of detection of recent ischemic stroke. These signal discrepancies also correspond to reduced water ADC in ischemic brain tissue due to cytotoxic oedema [3]. The smaller ADC values in the vicinity of the early-infarcted core are also indicative of tissue at risk of final infarction. Indeed, subtle ADC changes remain invisible on DWI, and early moderate decrease in ADC may occur in true penumbra. Extraction of the penumbra area from ADC maps within 6 h following stroke onset could help predict the infarct growth and, even more accurately, the final size of the infarct [4, 8, 10]. Further, DWI signal intensity depends on multiple factors such as the diffusion rate of molecules, T1 and T2 relaxation times, and local proton density. ADC, however, is independent of confounding T2 effects and ADC average or ''trace'' maps are also independent of diffusion anisotropy. Finally, ADC is an absolute measure expressed in $mm^2\ s^{-1}$, which is independent on the scanner [2].

2 Subjects and methods

The present study consisted of the development and pilot evaluation of a region growing segmentation technique of ADC maps dedicated to the extraction of brain areas likely to be affected by infarct within the next few days following stroke.

2.1 Patients

The patient population consisted of an initial database of 20 patients (age: mean 57, range [30, 73]; 100% without re-permeability) to tune the parameters of the method and a larger database of 77 patients (age: mean 59, range [26, 84]; with 49% complete, 22% partial, 29% without re-permeability) dedicated to its evaluation. These patients suffered from acute hemispheric stroke and were scanned with DWI within the 6 first hours following symptoms onset. ADC maps were obtained from DWI processing. A follow-up scan was performed within the next 1.2 days on average (range [0.5, 6.3]).

2.2 Imaging parameters

DWI scans consisted of 24 256×256 axial slices (5 mm thickness) with an inter-slice gap of 0.5 mm. Each axial slice was obtained with spin-echo multi-slice single-shot echo-planar imaging sequence with a baseline T2 acquisition ($b = 0\ s\ mm^{-2}$) and $b = 1{,}000\ s\ mm^{-2}$. ADC ''trace'' images were generated with a dedicated software tool (FuncTool, General Electric, Buc, France).

2.3 Image pre-processing

Original image processing tools were developed in C on a conventional Linux workstation under the brainVISA environment (http://www.brainvisa.info). Initial and follow-up scans were co-registered in the Talairach reference system and retrospective quantitative measurements were obtained from three pathophysiological regions of interests (ROI): (1) the volume of initial DWI abnormalities, which was considered as the ischemic core (CORE); (2) the final volume of the infarct (INF) taken from the final DWI abnormalities; and (3) the at-risk region or infarct growth area (IG), defined as the difference between INF and CORE ROIs. Mirror regions were also delineated for subsequent comparison with ADC values within contralateral healthy tissues. ADC maps were thresholded between 150 and $1{,}200\ mm^2\ s^{-1}$ to remove voxels contaminated with partial volume effects from cerebrospinal fluid. For each patient, all ROIs were manually delineated by the neurologist for quantitative comparison with the outcomes of the automatic segmentation procedure.

2.4 Image analysis and region-growing segmentation

The segmentation procedure is guided by a region-growing process as a modelling approach to the infarct growth. Initialization consists of the definition of a mask for the initial lesion obtained by expert neurologists using visual adaptive thresholding of the initial DWI (see [5] for automatic alternatives). Growth then runs through iterative voxel classification at the evolving infarct 3D envelope using voxel-based and region-based prior models of ADC intensity profiles in the INF region. These models are built on basic sample statistics of ADC values that were extracted from all ipsi and contralateral ROIs in the initial database (Table 1). Voxel classification is therefore achieved by alternatively considering the next voxel candidates as either ultimately belonging to the final infarct region or to healthy tissue. The numerical objective consists in minimizing a global energy index E computed over the set of voxels v in the INF region. Recent studies have demonstrated that the average and individual voxel ADC intensity values are significantly smaller in the INF region during the acute stage than in controlateral healthy tissues [6,11]. Therefore, E includes terms that relate to region and pixel-based properties (E_R and E_P, respectively) of the infarct volume and a regularizing feature, E_s, which ensures a smooth surface envelope to the infarct volume along iterations: $E = \alpha E_R + \beta E_P + \gamma E_S$. α, β and γ are scalar hyperparameters. The individual energy terms are defined as:

Table 1 Sample statistics of ADC intensity values obtained from the initial database ($N = 20$): region-based (average ADC values and standard deviations for each ROI) and voxel-based statistics (sample statistics of the voxel population in each ROI)

	ADC intensities					
	Region-based statistics			Voxel-based statistics		
ROI	CORE	IG	INF	CORE	IG	INF
Lesion	645 ± 75	823 ± 43	750 ± 69	690 ± 199	824 ± 174	772 ± 196
Mirror	840 ± 52	860 ± 36	851 ± 44	851 ± 167	860 ± 160	861 ± 156
Ratio	0.77	0.96	0.88	0.81	0.96	0.90

The mean ADC values of regions can further be compared with the values in the contralateral healthy hemisphere and expressed as an ADC ratio

$$E_R = \left(\frac{\bar{i}_{INF} - i_{INF}}{\sigma_{INF}}\right)^2, \quad \text{where } \bar{i}_{INF} = \frac{1}{N_{INF}} \sum_{v \in INF} i(v);$$

$$E_P = \sum_{v \in IG} \left(\frac{i(v) - i_{IG}}{\sigma_{IG}}\right)^2; \quad E_S = \sum_{v \in INF} \left(\frac{N_v - N/2}{\delta}\right)^\beta.$$

All voxel intensity values in E_R and E_P are expressed relatively to the average tissue intensity in the contralateral healthy region (see Sect. 3). $\bar{i}_{INF}$ is the average ADC intensity in the current INF region; i_{INF} (res. σ_{INF}) is a prior on the expected average (res. tolerance) ADC intensity in the final INF region. $i(v)$ is the ADC intensity at voxel v. $\bar{i}_{IG}$ (res. σ_{IG}) is also a prior on the expected ADC intensity (res. standard deviation) at the voxel level for voxels in IG. N_{INF} (res. N_{IG}) are the current counts of voxels in the INF and IG regions, respectively. E_S is the Ising regularization functional: N is the total number of

voxel neighbours (e.g. 26) out of which N_v belong to INF. δ and β are fixed scalar parameters. Global optimization is run iteratively on each element v_0 of the voxel front according to: $v_0 \in \text{INF} \Leftrightarrow E_{v_0 \in \text{INF}} < E_{v_0 \notin \text{INF}}$. Growth is complete when no more voxels are acceptable in the INF region. Infarct growth was considered as significant if the IG volume was superior to 10 cm^3. Performances of our method were then evaluated in terms of specificity and sensitivity of infarct growth prediction and compared with those generally observed from the perfusion–diffusion mismatch alternative approach.

3 Results

The average volume of the infarct lesions in the initial database increased from 36 ± 26 cm^3 (CORE) to 96 ± 81 cm^3 (INF). In the hemisphere ipsilateral to the infarct, ADC intensity values revealed significant differences between all 3 ROI types, while as expected, no difference were detected between the corresponding mirror ROIs in the healthy hemisphere (Table 1). Our study confirms that average ADC values are significantly smaller in CORE than in INF [10].

In the final evaluation database (N = 77), the volume of the lesion increased from 40 ± 36 cm^3 to 81 ± 72 cm^3, (mean growth: 41 ± 50 cm^3). The average final infarct volume predicted by our method was 79 ± 72 cm^3, with significant correlation with the true final volumes (resp. infarct growth) at the population level: r = 0.71 (resp. r = 0.56; Fig. 1a), $P < 0.0001$.

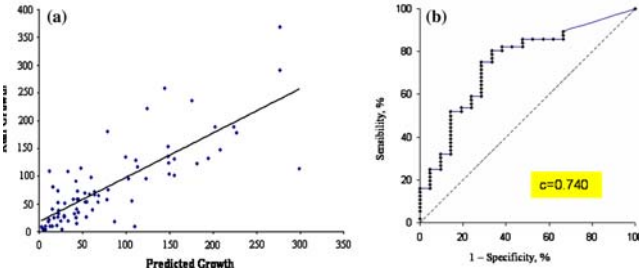

Fig. 1 **a** Real vs. predicted infract growth volumes. **b** ROC analysis of the performances from the automatic prediction method. **c** Area under the curve

Automatic prediction of the infarct growth performed with 75% sensitivity and 71% specificity scores. ROC analysis revealed a satisfactory measure of the area under the curve index (c = 0.74, Fig. 1b). These performances are comparable to the ones achieved by the perfusion–diffusion mismatch approach, though this latter necessitates the monitored injection of a contrast agent in the scanner, a heavy constraint in the context of absolute emergency. Convergence of the iterative algorithm was fast (< 10 min on average, on a conventional workstation). The method is exemplified Fig. 2.

4 Conclusions

Because the ADC values reflect the ischemic history of the tissue, this parameter was confirmed to be predictive of final tissue outcome. We have shown in this study that automatic segmentation of the ADC profile from early scans is reliable, fast, and no-invasive. Segmentation was achieved by a region-growing procedure that includes limited a priori knowledge about the infarcted area: the expected average ADC value—derived from the retrospective analysis on a limited population of patients—and smooth surface envelopes priors. These are encouraging results for the fast and automatic segmentation of ADC maps in the anticipation of infarct growth and represent an alternative to the still-debated perfusion–diffusion mismatch approach. Ongoing research includes refinement of the segmentation procedure to achieve greater quantitative accuracy by including extended knowledge on brain vascular structure and comprehensive investigation of the 3D ADC profile.

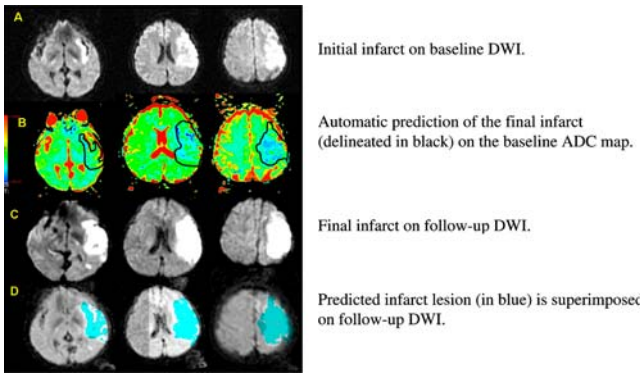

Fig. 2 An example of the automatic prediction in a patient with initial infarct volume of 81.9 cm^3 (**a**), the real final infarct volume is 130.4 cm^3 (**c**), and the predicted final volume was 154.9 cm^3 (**b**, **d** with blue mask). True (resp. predicted) growth is 48.5 cm^3 (resp. 68.0 cm^3)

References

1. Connelly A, Calamante F, Porter DA, Gadian DG (2000) Case study on diffusion and perfusion magnetic resonance imaging in childhood stroke. Electromedica Neuro 68:2–8
2. Cosnard G, Duprez T, Grandin C et al (1999) Imagerie de Diffusion et de Perfusion par Résonance Magnétique de l'Encéphale. Louvain Med 118:129–140
3. Fiebach JB, Jansen O, Schellinger PD et al (2002) Serial analysis of the apparent diffusion coefficient time course in human stroke. Neuroradiology 44:294–298
4. Gass A, Hirsch JG, Behrens S et al (2000) Exemplary studies on diffusion and perfusion weighted magnetic resonance imaging in acute neurological disease. Electromedica 2(68):106–111
5. Li W, Tian J, Li E, Dai J (2004) Robust unsupervised segmentation of infarct lesion from diffusion tensor MR images using multiscale statistical classification and partial volume voxel reclassification. NeuroImage 23:1507–1518
6. Na DG, Thijs VN, Albers GW et al (2004) Diffusion-weighted MR Imaging in acute ischemia value of apparent diffusion coefficient and signal intensity thresholds in predicting tissue at risk and final infarct size. AJNR Am J Neuroradiol 25:1331–1336
7. Nagesh V, Welch KMA, Windham JP et al (1998) Time course of ADC_w changes in ischemic stroke: beyond the human eye! Stroke 29:1778–1782
8. Oppenheim C, Stanescu R, Dormont D et al (1999) Diffusion MRI and cerebral ischemia. When to calculate the coefficient of diffusion? J Neuroradiol 26(4):242–248
9. Oppenheim C, Samson Y, Manaï R et al (2000) Prediction of malignant middle cerebral artery infarction by diffusion-weighted imaging. Stroke 31:2175–2181
10. Oppenheim C, Grandin C, Samson Y et al (2001) Is there an apparent diffusion coefficient threshold in predicting tissue viability in hyperacute stroke? Stroke 32:2486–2491
11. Shaefer PW, Ozsunar Y, He J et al (2003) Assessing tissue viability with MR diffusion and perfusion imaging. AJNR Am J Neuroradiol 24:436–446
12. Warach S (2001) Tissue viability thresholds in acute stroke: the 4-factor model. Stroke 32:2460–2461